



# Joint Inversion of 1-D Magnetotelluric and Surface-Wave Dispersion Data with an Improved Multi-Objective Genetic Algorithm and Application to the Data of the Longmenshan Fault Zone

PINGPING WU,<sup>1,2,3</sup>  HANDONG TAN,<sup>1,2</sup> MIAO PENG,<sup>1,2</sup> HUAN MA,<sup>3</sup> and MAO WANG<sup>1,2</sup>

**Abstract**—Magnetotellurics and seismic surface waves are two prominent geophysical methods for deep underground exploration. Joint inversion of these two datasets can help enhance the accuracy of inversion. In this paper, we describe a method for developing an improved multi-objective genetic algorithm (NSGA-SBX) and applying it to two numerical tests to verify the advantages of the algorithm. Our findings show that joint inversion with the NSGA-SBX method can improve the inversion results by strengthening structural coupling when the discontinuities of the electrical and velocity models are consistent, and in case of inconsistent discontinuities between these models, joint inversion can retain the advantages of individual inversions. By applying the algorithm to four detection points along the Longmenshan fault zone, we observe several features. The Sichuan Basin demonstrates low S-wave velocity and high conductivity in the shallow crust probably due to thick sedimentary layers. The eastern margin of the Tibetan Plateau shows high velocity and high resistivity in the shallow crust, while two low velocity layers and a high conductivity layer are observed in the middle lower crust, probably indicating the mid-crustal channel flow. Along the Longmenshan fault zone, a high conductivity layer from  $\sim 8$  to  $\sim 20$  km is observed beneath the northern segment and decreases with depth beneath the middle segment, which might be caused by the elevated fluid content of the fault zone.

**Key words:** Magnetotellurics, surface wave, joint inversion, NSGA-SBX.

## 1. Introduction

Magnetotellurics (MTs) is one of the main geophysical methods used to derive conductivity of the

lithosphere from time-varying electromagnetic fields analysis (Tikhonov 1950; Cagniard 1953; Egbert and Booker 1992), while measurements of surface-wave dispersion provide the most important information on thickness and velocity ( $V_p$ ,  $V_s$ ) of the lithosphere on both regional and global scale (Nelson et al. 1996; Ritzwoller and Levshin 1998; Wu and Levshin 1994; Li et al. 2009a, b). The combination of these two methods is proven to be essential for imaging deep crustal and upper mantle structures in complex geological terranes. Nevertheless, due to geological heterogeneity and model non-uniqueness, significant differences are commonly found between velocity and electrical models inverted independently. Joint inversion can simultaneously obtain a variety of physical properties, which can improve the discrimination of the geology structure and the dynamic mechanism. In addition to conducting joint inversion based on the direct relationships among physical parameters (Dobroka et al. 1991; Arie et al. 1997; Colombo and Stefano 2007), other approaches have shown that using the cross-gradient of the electrical and velocity models as constraints provides an effective structural coupling between different physical parameters (Gallardo and Meju 2003, 2004). However, the cross-gradient method, which requires different gradient directions of parameters, is not applicable to 1-D joint models in which the changes in velocity and resistivity are aligned.

In recent decades, multi-objective evolutionary algorithms have been recognized as being effective and efficient, as their population-based property can obtain an approximation of a Pareto-optimal set in a single run (Srinivas and Deb 2000; Knowles and Corne 1999; Zitzler 1999). Moorkamp et al. (2011)

<sup>1</sup> Key Laboratory of Geo-Detection, China University of Geosciences, Ministry of Education, Beijing 100083, China. E-mail: wupingping2010@163.com

<sup>2</sup> School of Geophysics and Information Technology, China University of Geosciences, Beijing 100083, China.

<sup>3</sup> Institute of Disaster Prevention, Hebei 101601, China.

and Roux et al. (2011) applied the non-dominated sorting genetic algorithm (NSGA) to the joint inversion of receiver functions, surface-wave dispersions, and magnetotelluric datasets to illustrate the velocity and electrical structure of the lithosphere, with an encoded binary form that mimics survival of the fittest in biological evolution. This method comprises a specific discretization process, which can cause a number of difficulties like the inability to achieve arbitrary precision in the obtained solutions, fixed mapping of problem variables, inherent Hamming cliff problems associated with the binary coding, computational load, and resolution (Kalyanmoy and Agarwal 1995; Kalyanmoy et al. 2002). The real-coded approach in genetic evolution has been found to be more suitable for dealing with optimization problems of continuous parameters within the earth. In particular, simulated binary crossover (SBX) was designed to deal with continuous multi-objective optimization problems and works effectively to enhance the search capability of multi-objective evolutionary algorithms (Kalyanmoy and Agarwal 1995). Kalyanmoy et al. (2002) found that NSGA with SBX (NSGA-SBX), in comparison with the Pareto-archived evolution strategy, is able to find a much better spread of solutions and better convergence near the true Pareto-optimal front compared with the Pareto-archived evolution strategy in a set of difficult test problems.

Since the NSGA algorithm with SBX can yield better convergence results and can also effectively avoid the problems caused by the traditional genetic method with binary encoding, we apply this method to the joint inversion of surface-wave dispersion (SWD) and MT datasets in this study. Two numerical examples are tested to verify the accuracy and advantages of the joint inversion algorithm in the case of consistent or inconsistent discontinuities between velocity and electrical models. Finally, four detection points along the Longmenshan fault zone are used to verify the robustness of NSGA-SBX, and identify the velocity and resistivity structure associated with different tectonic blocks (Tibetan Plateau, Sichuan Basin, northern and middle of the Longmenshan Fault).

## 2. Method

The multi-objective genetic algorithm can simultaneously process both MT and SWD datasets without selecting a weighting factor between them. During the inversion process, NSGA-SBX solves the multi-objective problem by storing the parameters of velocity, resistivity, and thickness in a vector. The coupling between velocity and electrical models is achieved using a common set of thickness values for the inversion layers.

Figure 1 is the flow chart for the NSGA-SBX method. In the program, five main steps are included: ① non-dominated sorting helps to find the optimal Pareto front models, and the models of the first rank in the final generation are treated as the optimal results of the inversion; ② crowding distance measures how close an individual is to its neighbors, which helps to ensure the diversity of the populations; ③ after the individuals are sorted using non-dominated sorting and crowding distance, the individuals for GA process are carried out using Tournament Select; ④ SBX genetic operators (crossover and mutation) are used to create offsprings for the evolution of the populations; ⑤ finally, to balance the RMS between SW and MT data sets, we select the trade-off of the first rank models in the final generation as the optimal model. A full description of these steps can be found in past studies (Moorkamp et al. 2011), except for the SBX genetic process, which is described in detail below.

Unlike traditional genetic operators, SBX genetic operators only have to specify the maximum and minimum value for each parameter in the models, regardless of the discretization process and the number of bits used for encoding. SBX simulates the binary crossover and mutation observed in nature. The formulas of crossover are given as follows:

$$C_{1,k} = \frac{1}{2} [(1 - \beta_k)p_{1,k} + (1 + \beta_k)p_{2,k}], \quad (1)$$

$$C_{2,k} = \frac{1}{2} [(1 + \beta_k)p_{1,k} + (1 - \beta_k)p_{2,k}], \quad (2)$$

and

$$\beta_k(\mu) = (2\mu)^{\frac{1}{n_k+1}}, \text{ if } \mu \leq 0.5, \quad (3)$$

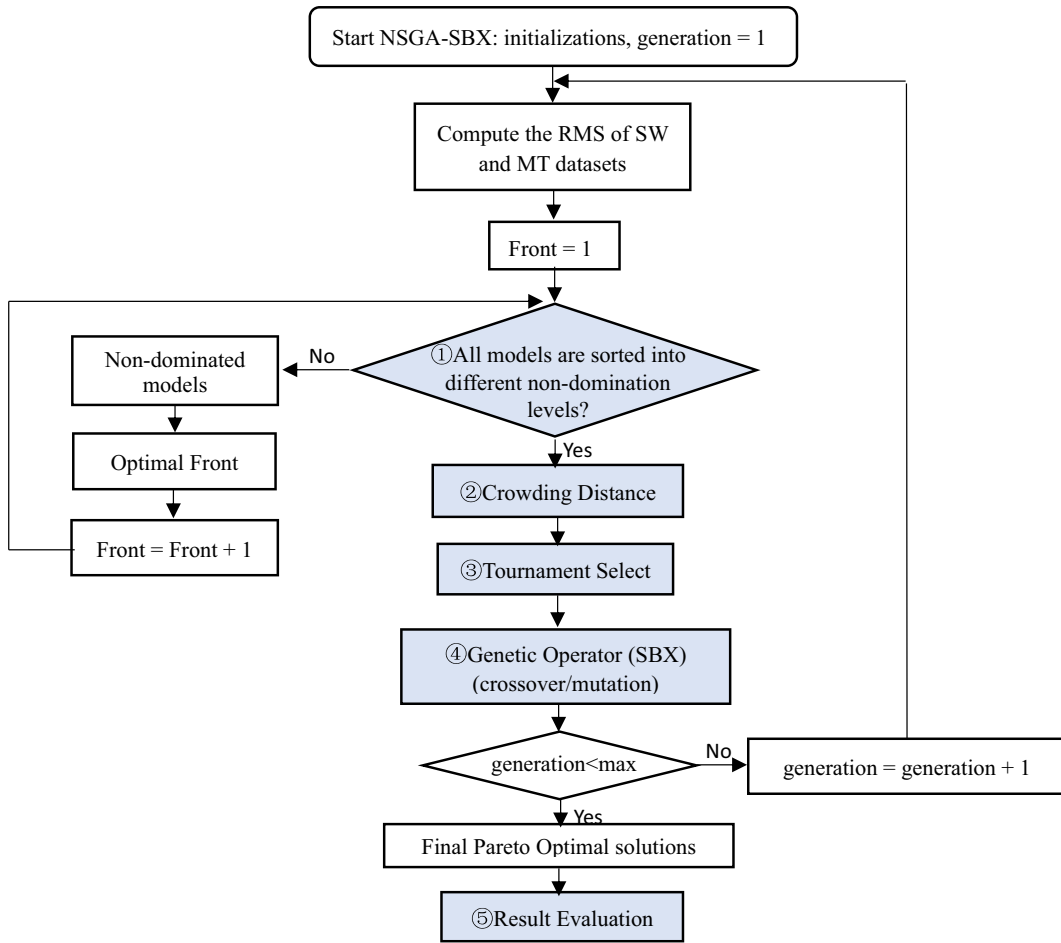


Figure 1  
Flow chart for the NSGA-SBX method

$$\beta_k(\mu) = \frac{1}{(2 - 2\mu)^{\frac{1}{\eta_c + 1}}}, \text{ if } \mu > 0.5, \quad (4)$$

where  $C_{i,k}$  is the  $i$ th child with  $k$ th individual or model,  $p_{i,k}$  is the selected parent, and  $\eta_c$  is the distribution index for crossover. Distribution  $\beta$  can be obtained from a uniformly sampled random number between  $\mu(0,1)$ .

The formulas of mutation are

$$C_k = p_k + (p_k^u - p_k^l)\delta_k, \quad (5)$$

and

$$\delta_k = (2r_k)^{\frac{1}{\eta_m + 1}} - 1, \text{ if } r_k < 0.5, \quad (6)$$

$$\delta_k = 1 - (2 - 2r_k)^{\frac{1}{\eta_m + 1}}, \text{ if } r_k \geq 0.5, \quad (7)$$

where,  $c_k$  is the offspring and  $p_k$  is the parent, and  $p_k^u$  and  $p_k^l$  represent the upper and lower bounds of each parameters, respectively; moreover,  $r_k$  is a uniformly sampled random number between  $(0,1)$ ,  $\eta_m$  is a mutation distribution index,  $\delta_k$  is a small variation, which is calculated from a polynomial distribution using  $r_k$ . In this paper, both  $\eta_c$  and  $\eta_m$  are set to the value of 20.

From the formulas of SBX processing (from Eqs. 1 to 7), we can see that the individuals generated from crossover and mutation in genetic evolution are continuous between the maximum and minimum values of each parameter, since the value of  $\beta$  and  $\delta$  can be obtained from a polynomial distribution; while in the traditional genetic process, the individuals

should be converted to binary form by the discretization step within the scope, then cross and mutate in the binary domain, and finally reconverted to decimal form to generate new individuals. Compared with SBX, the binary encoding process needs to convert between decimal and binary domains, which might lead to computer load increase. Moreover, the selection of discretization step impacts the accuracy and stability of inversion results. The following section introduces the results of the comparison of these two methods.

### 3. Synthetic Tests

#### 3.1. Models with Consistent Discontinuities in Velocity and Resistivity

In forward modeling, we set up two three-layer models in this test, specifying 2 km for the thickness of the first and second layer and half space for the third layer. In the setting of velocity, we design a linear increment model with 20% abnormality in the second layer. Two electrical models are set for joint inversion with one common velocity model, which, under the same background resistivity (100  $\Omega$  m), respectively, display low resistivity (10  $\Omega$  m) and high resistivity (300  $\Omega$  m) in the middle layer. Figure 2 shows the synthetic Rayleigh wave group velocity, MT apparent resistivity and phase datasets.

In the inversion process, we specify the parameters as follow: *S*-wave velocity ranges between 1.0 and 4.0 km/s and resistivity ranges from  $2^{-8}$  to  $2^{10}$   $\Omega$  m. The genetic algorithm creates random populations of a fixed size (500) with a number of iterations of 100.

Figure 3 show the inversion results. The evolution models of the first Pareto front are shown in Fig. 3a during iterations in the joint inversion of the low velocity and low resistivity models. The black dots represent the optimal models in the final iteration. The Pareto-optimal models are shown in Fig. 3b in black lines, and we identify that the clustering of the models matches well with the real model (red lines in Fig. 3b). The yellow pentagram in Fig. 3a represents the trade-off of the final optimal models mentioned in Sect. 2. Its corresponding model is shown in yellow

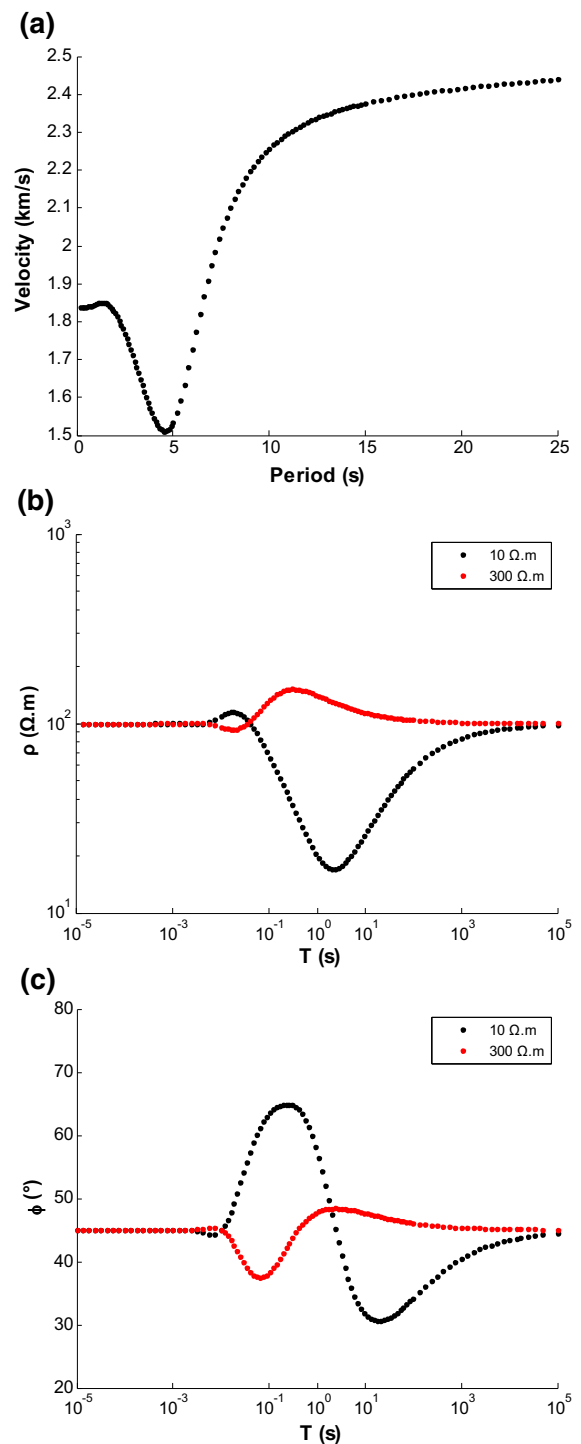
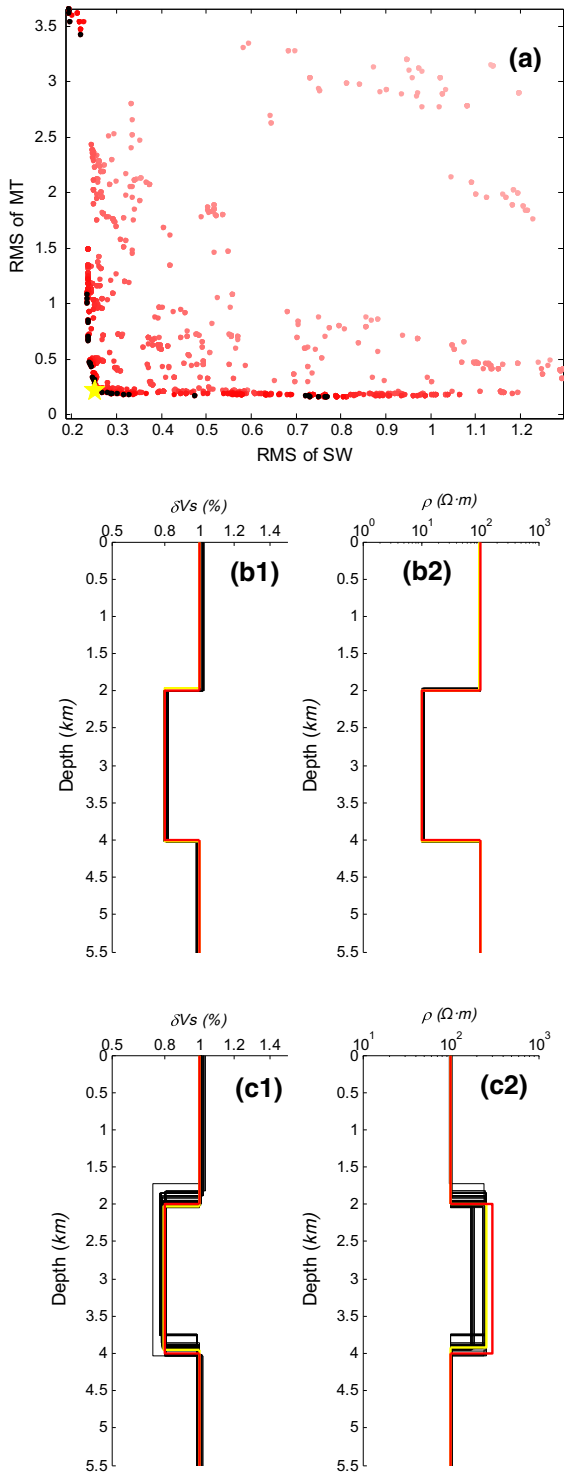


Figure 2 Synthetic surface dispersion datasets (a), apparent resistivity (b) and phase datasets (c). Black and red lines in b, c represent the synthetic apparent resistivity and phase curves of the models with low resistivity (10  $\Omega$  m) and high resistivity (300  $\Omega$  m) in the middle layer, respectively



◀Figure 3

**a** Evolution of Pareto front during iterations in joint inversion of the low velocity and low resistivity models, **b** joint inversion results of the low velocity and low resistivity models, **c** joint inversion results of the low velocity and high resistivity models. Red dots from shallow to deep in color represent the evolution of Pareto front in each generation; black dots represent the final optimal Pareto front models; yellow pentagram represents the trade-off of the final optimal Pareto front models; black lines in **b**, **c** represent the optimal models in the final Pareto front; red lines in **b**, **c** represent the real model, yellow lines represent the corresponding models of the trade-off

and high resistivity models. Moreover, we can clearly find that the clustering of the final optimal models is focused within a small range near to the real model (red line in Fig. 3c), although the inversion accuracy is lower than the results of the low resistivity model (Fig. 3b), which can be explained by MT datasets being more sensitive to low resistivity anomalies.

To compare the inversion results with SBX and binary encoding, we specify the different discretization steps (Table 1) based on the model in Fig. 3b. The inversion results are shown in Fig. 4. Figure 4a–c illustrate the inversion results from the parameters of P1, P2 and P3 in Table 1, respectively. The results clearly indicate that the stability and reliability of the inversion results vary with different discretization steps. When the selected discretization steps are suitable, the inversion results can be well revealed (Fig. 4a). In the other case, the inversion results are unstable when the selected discretization steps are not coordinated (Fig. 4b, c). In contrast, the results from the SBX method (Fig. 3b) used in this paper show better convergence and higher precision, suggesting

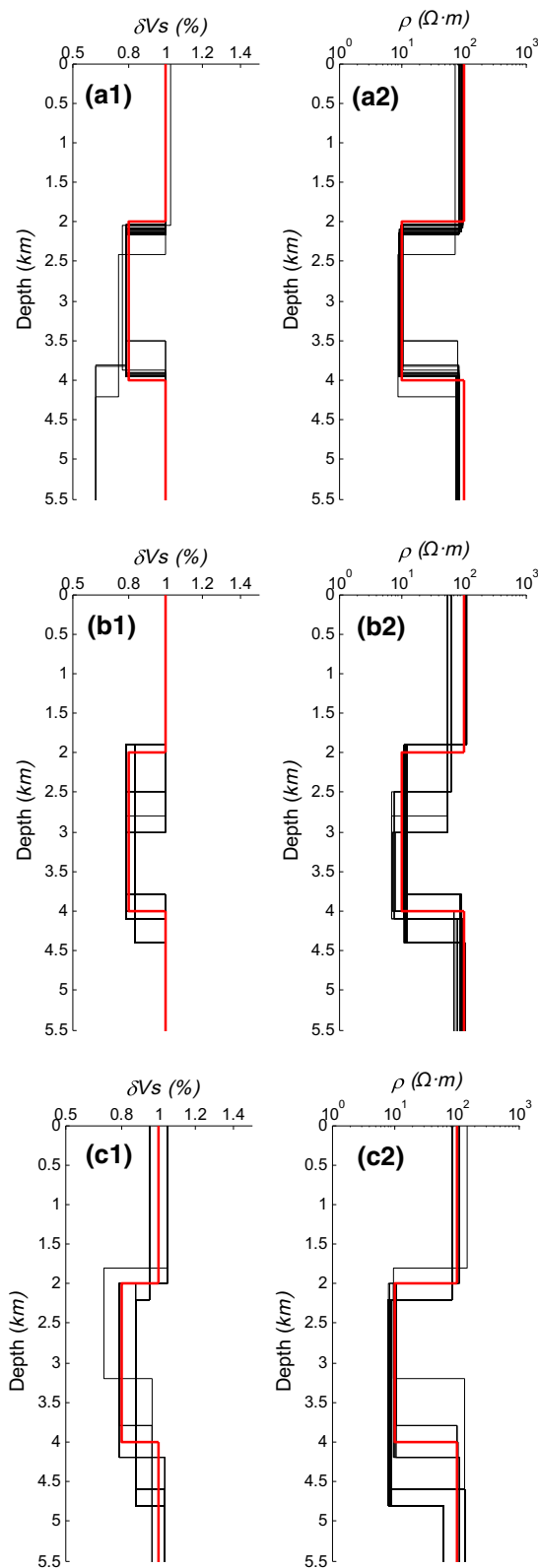
Table 1

*Three different discretization steps of thickness, velocity and resistivity for joint inversion in binary encoding process*

Parameters	P1	P2	P3
$\Delta H$ (km)	0.01	0.3	0.2
$\Delta V_s$ (km/s)	0.05	0.1	0.2
$\Delta \rho$ ( $\Omega \cdot m$ )	$2^{0.1}$	$2^{0.1}$	$2^{0.1}$

$\Delta H$ ,  $\Delta V_s$  and  $\Delta \rho$  the discretization steps of thickness, velocity and resistivity, P1, P2, P3 the three different discretization steps for joint inversion in Fig. 4a, b, c, respectively

lines in Fig. 3b (notice that all the yellow lines in the following figures represent this model). Figure 3c shows the joint inversion results of the low velocity



◀Figure 4

Joint inversion results with different discretization steps in genetic evolution. **a** Joint inversion results with the discretization steps 0.01 km in thickness, 0.05 km/s in shear wave velocity, and  $2^{0.1}$   $\Omega$  m in resistivity; **b** joint inversion results with the discretization steps 0.3 km in thickness, 0.1 km/s in shear wave velocity, and  $2^{0.1}$   $\Omega$  m in resistivity; **c** joint inversion results with the discretization steps 0.2 km in thickness, 0.2 km/s in shear wave velocity, and  $2^{0.1}$   $\Omega$  m in resistivity

that this new inversion technique can effectively avoid the problems caused by the binary encoding process.

### 3.2. Models with Inconsistent Discontinuities in Velocity and Resistivity

In many cases, velocity discontinuities can be inconsistent with the electrical structure. To check whether our algorithm is applicable to this case, we set up two five-layer models for testing. The red lines in Fig. 5a represent the velocity and electrical models of the first model, in which two low velocity zones are observed in the second and fourth layer (Fig. 5a1), while the electrical structure from the second to fourth layer shows low resistivity (Fig. 5a2). Figure 5b shows the second model, in which the red lines indicate that two low resistivity zones exist in the second and fourth layer (Fig. 5b2) and a thick low velocity zone extends from the second to fourth layer (Fig. 5b1).

The black lines in Fig. 5 represent the final optimal Pareto models. Overall, the clusters of the models are similar to those of the real models. Figure 5a1, a2 show the joint inversion results of the first model. Two layers of low velocity are clearly present, despite higher precision in the second layer than in the fourth one, and a thick low resistivity layer is observed from 2 to 7.5 km. In the second model, from Fig. 5b1, b2, a thick low velocity layer is observed from 2 to 8 km, and low resistivity is observed in the second and the fourth layer.

The synthetic tests demonstrate that the values of resistivity and velocity are independent of each other during the joint inversion process in spite of the use of a common set of thickness. In the presence of inconsistent discontinuities between velocity and

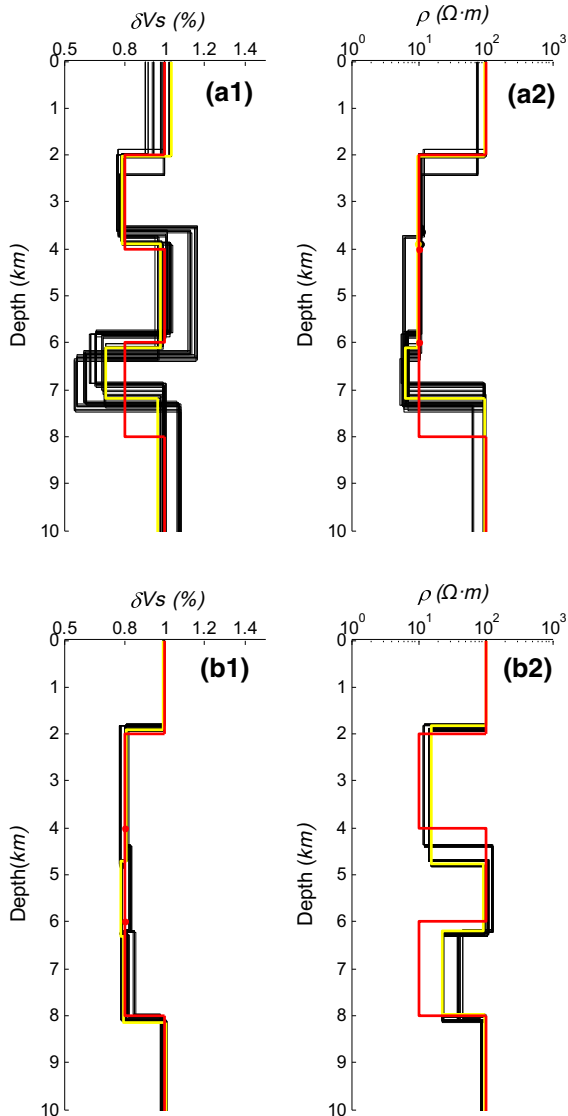


Figure 5

Joint inversion results for the models with inconsistent discontinuities in velocity and resistivity. Red lines represent the real model; yellow lines represent the corresponding model of the trade-off

electrical structures at the same depth, the value of velocity will vary greatly to exhibit the interface, while the value of resistivity changes slightly, showing continuity, which effectively retains the advantages of individual inversions. In contrast, when there exists one or more coupling interfaces in velocity and electrical models, the inversion result can be improved by the integrated data sets.

#### 4. Application

Located between the Tibetan Plateau and the Sichuan Basin, the Longmenshan fault zone plays an important role as a mechanism of building topography. One of the mechanisms suggested by Clark and Royden (2000) is the crustal flow model. The southeast-directed crustal flow beneath the central plateau is blocked by the stable lithosphere beneath the Sichuan Basin, leading to the narrow, steep topographic margin between the plateau and the basin. In recent years, numerous studies have been conducted to confirm this model from seismic analysis (Li et al. 2009a, b; Liu et al. 2014; Wu et al. 2009) and MT analysis (Wang et al. 2009; Peng et al. 2015; Zhao et al. 2012). However, these studies are limited to individual inversions.

To simultaneously reveal velocity and electrical structures, we adopt the NSGA-SBX method to explore the deep structures along the Longmenshan fault zone. Figure 6 shows the locations of the MT points and the SW points; as shown, the four detection points are located in four different tectonic areas: point 1 is in the eastern margin of Tibetan Plateau, with obvious topographical differences as compared to point 3 located in the Sichuan Basin; point 2 and point 4 are located in the middle and northern part of the Longmenshan fault zone, respectively.

Li et al. (2009a, b) extracted the group velocity dispersion curves for each grid node of the  $0.2^\circ \times 0.2^\circ$  from long time noise cross-correlation of continuous seismogram between station pairs in western Sichuan and eastern Tibet. Four points of the grids (Fig. 6 red triangles) near to the MT sites (black triangles in Fig. 6) are used in this paper. Figure 7 shows the dispersion curves of the four points. As Fig. 7 shows, group velocity dispersion curves nearly overlap at point 2 and point 4, which might suggest similar velocity beneath the two points. As we can be seen with points 1, 2 and 3 across the Longmenshan fault zone, the group velocity decreases from west to east in the period between 5 and 25 s which probably suggests significant differences in velocity structure in the shallow crust beneath different tectonic blocks around the Longmenshan fault zone.

The non-uniformity of the medium leads to differences in the impedances from different azimuth



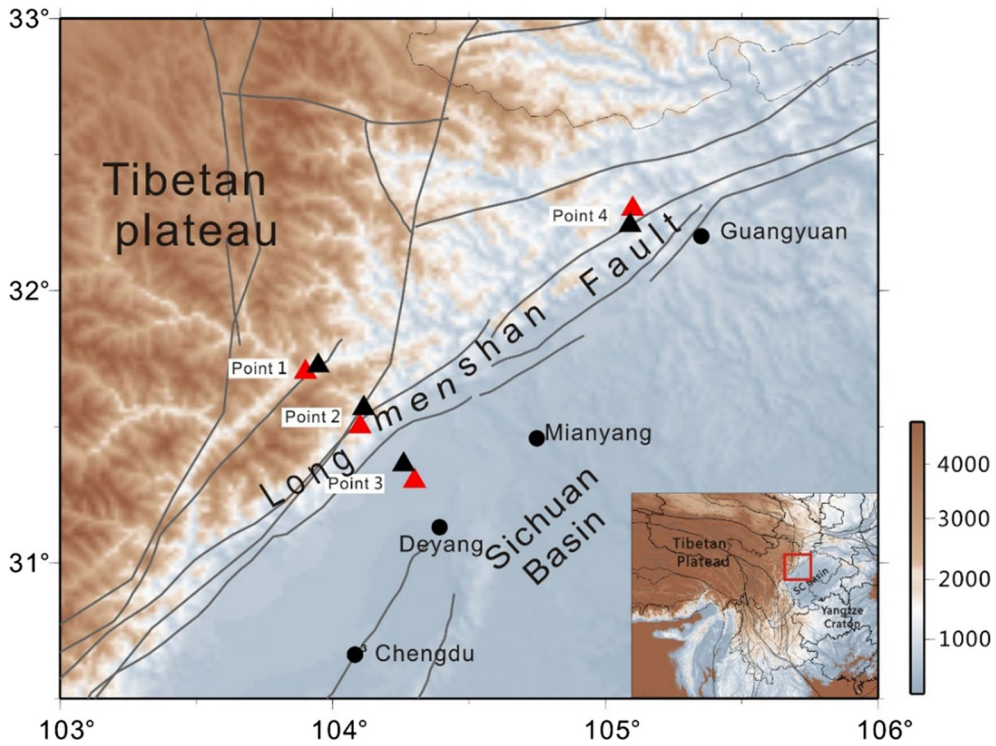


Figure 6

Locations of the detected MT and SWD points. Red triangles represent the locations of the SWD datasets; the black triangles represent the locations of the MT datasets; and the black circles represent the locations of cities in the study area

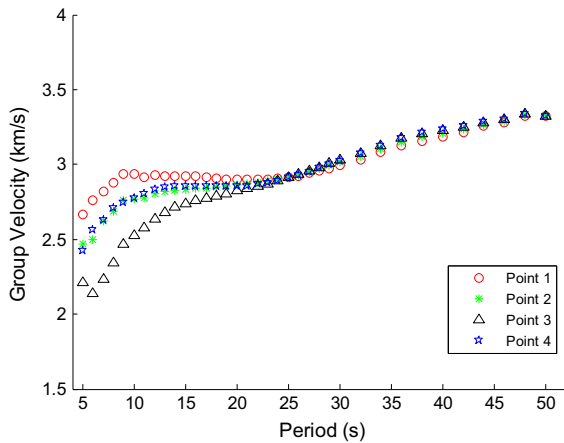


Figure 7

Group velocity dispersion curves of the four points (Li et al. 2009a, b)

measurements in MT observation. The black dots and green dots in Fig. 8 represent the apparent and phase curves in the TE mode and TM mode, respectively. Despite only partial overlap of the MT datasets of the

two modes, the trends are almost identical. Here, we apply the Berdichevskiy analyses for the MT datasets to reduce the influence of the inhomogeneity of the medium. The blue dots in Fig. 8 represent the curves dealt within the Berdichevskiy method. The Rhoplus method (Parker and Booker 1996) is then adopted to check the consistency of the apparent resistivity and phase curves. The red circles in Fig. 8 represent the curves after Rhoplus analysis. In these curves, the electrical structures exhibit a clear “high–low–high” resistivity as depth increases beneath point 1, and “low–high” resistivity beneath point 3. At point 2, resistivity increases with the wave period, while the phase curve first decreases and then increases. The changes in resistivity and phase curve at point 4 are opposite to those at point 2.

Considering that the scale of the low velocity abnormal layer beneath the eastern Tibetan Plateau is approximately 25 km and that in the shallow crust of the Sichuan basin, it is approximately 8 km (Li et al.



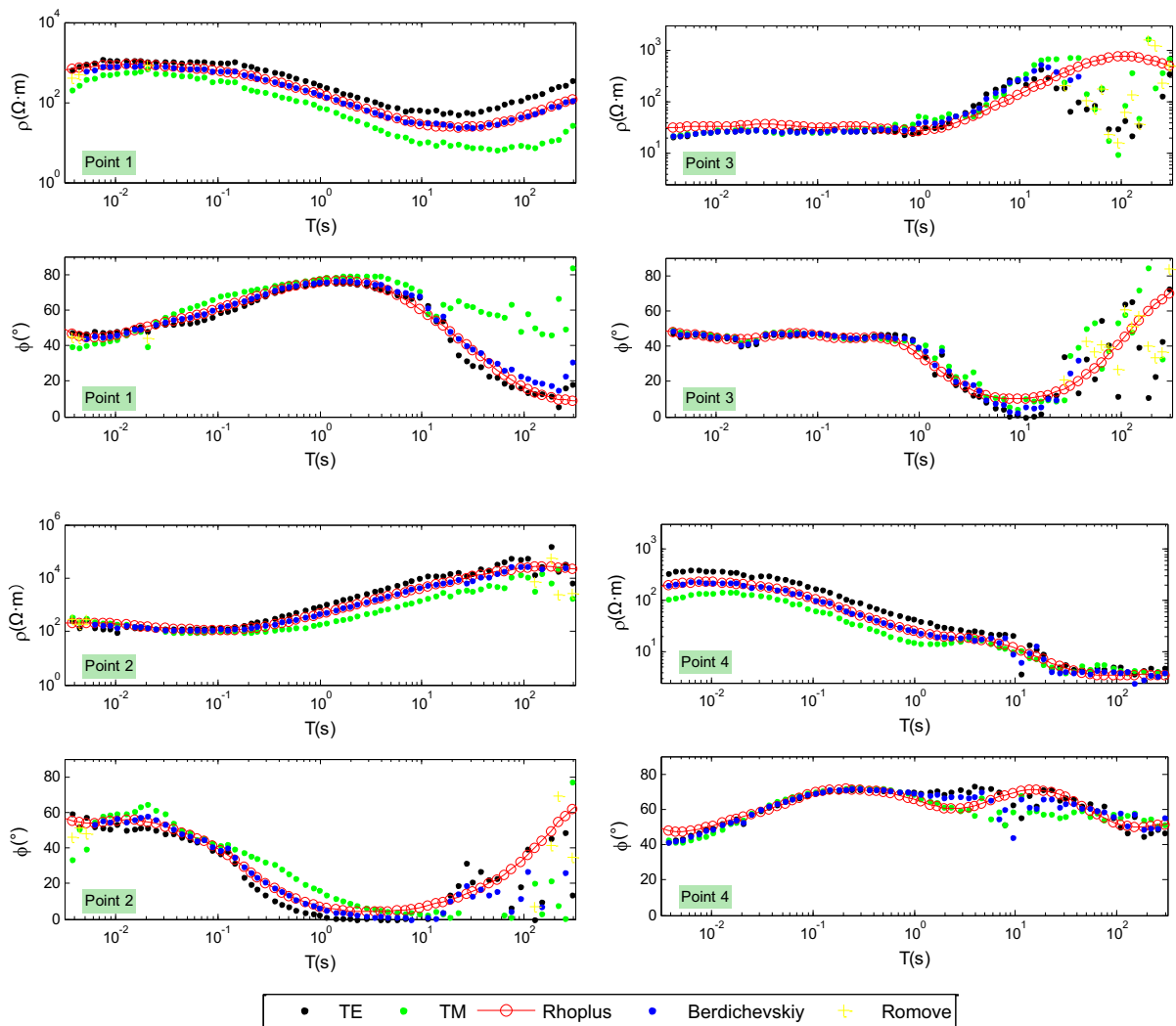


Figure 8

Data processing of the four MT points. Black dots represent the apparent resistivity and phase curves of the TE mode; green dots represent the apparent resistivity and phase curves of the TM mode; blue dots represent the curves dealt with the Berdichevskiy method; red circles represent the results analyzed by the Rhoplus method; yellow crosses represent the removed data points

2009a, b), we set the thickness of each layer for inversion in a range of 1–30 km to ensure that the anomalous bodies can be fully covered. As the target depth in the study is  $\sim 60$  km and the median of the thickness scope is 15 km, we set up two five-layer models for inversion. The scopes of velocity and resistivity have also been set as wide as possible to cover the anomaly, with  $2^{-6}$ – $2^{13}$   $\Omega$  m for resistivity and 2.0 and 5.0 km/s for S-wave velocity. The black lines in Fig. 9 represent the final optimal models of velocity (a1–d1) and resistivity (a2–d2) and their

corresponding forward MT apparent resistivity curves (a3–d3), phase curves (a4–d4) and SWD curves (a5–d5). The yellow lines represent the trade-off model and its corresponding forward datasets. Overall, the yellow lines are consistent with the detected data sets (red lines in Fig. 9), and the final optimal models. These results show the effectiveness of NSGA–SBX and the reliability of the inversion results.

In comparing the velocity and electrical models in the four different blocks, we identify several features.

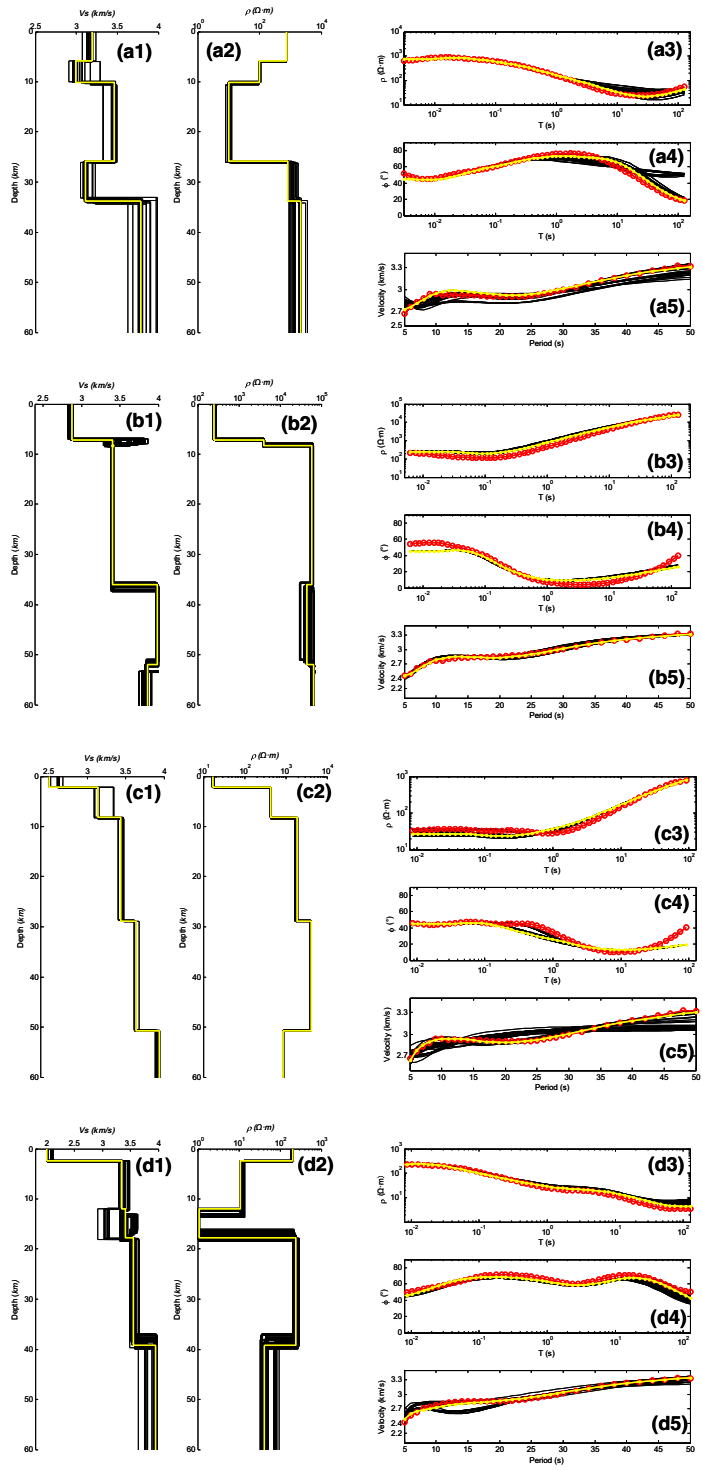


Figure 9

Inversion results of the four detection points. **a-d** Represent the joint inversion results at point 1, point 2, point 3 and point 4 respectively. **a1-d1**, **a2-d2** represent the velocity and electrical models of the final optimal Pareto results; **a3-d3**, **a4-d4**, **a5-d5** represent the forward curves of MT apparent resistivity, phase and SW group velocity dispersion datasets, respectively; yellow lines represent the models of the trade-off and their forward datasets; red lines represent the detected datasets

In point 1 located in the eastern margin of Tibetan Plateau, we observe a high velocity ( $\sim 3.2$  km/s) and high resistivity layer ( $\sim 10^3 \Omega \text{ m}$ ) in the shallow crust ( $\sim 7$  km); two low velocity ( $\sim 3.0$  km) layers and a high conductivity ( $\sim 10 \Omega \text{ m}$ ) layer are observed from  $\sim 8$  to  $\sim 32$  km, and high velocity ( $\sim 4$  km/s) and high resistivity ( $\sim 10^{3.2} \Omega \text{ m}$ ) is imaged over  $\sim 32$  km. In point 3 located in the Sichuan Basin, we observe a layer of low velocity ( $\sim 2.5$  km/s) and high conductivity ( $\sim 10 \Omega \text{ m}$ ) at about  $\sim 3$  km, and as depth increases, velocity increases while conductivity decreases. The velocity structures beneath point 2 and point 4 are nearly identical in spite of a lower velocity ( $\sim 2.8$  km/s at point 2 and  $\sim 2.0$  km/s at point 4) in the shallow crust beneath point 2. In addition, a high conductivity (lower than  $\sim 10^1 \Omega \text{ m}$ ) layer is observed from  $\sim 3$  to  $\sim 20$  km beneath point 4, and an extremely high resistivity ( $\sim 10^5 \Omega \text{ m}$ ) appears at  $\sim 8$  km beneath point 2.

From the fitting curves and concentrations of the final optimal models, the NSGA-SBX method is proven to be effective in the real datasets and can achieve highly accurate inversion results by simultaneously processing multi-geophysical datasets. Obvious differences can be found after analyzing the velocity and electrical structures, and are discussed in the following section.

## 5. Discussion

The integration of multiple geophysical parameters can successfully reconstruct the seismic velocity and electrical model at different depths with a higher degree of reliability than single inversion methods can achieve. In the numerical example of Sect. 3.1, two contents are included. First, when the discontinuities are consistent in velocity and electrical models, the inversion results can be improved by structure coupling constraints with the SWD and MT datasets. Generally, the inversion results tend to be more accurate in seismology than in electromagnetism. The high resolution of velocity model is represented by SWD, and electrical structure can be determined by MT datasets. From Fig. 3b, c, the low resistivity and high resistivity models can be well

inverted under the constraints of the same velocity model (Fig. 3b, c). Second, we compare the SBX and binary encoding in genetic evolution. In Figs. 3b and 4, we can clearly find that the results from SBX have better convergence, while the results from the binary encoding process are unstable, as the discretization steps of the inversion parameters (Fig. 4) change. The inversion results can be well revealed (Fig. 4a) when the selected discretization steps are coordinated. However, in many cases, it is difficult to find the optimal discretization steps due to the uncertainty of factors (e.g., the prior information, data quality) in different study areas. In contrast, the results processed by NSGA-SBX have better convergence to the real model (Fig. 3b). Based on the simulated crossover method, any solution between the maximum and the minimum value of each parameter can be identified as the result, thus overcoming the limitations with discretization steps in the binary encoding process.

The numerical testing in Sect. 3.2 aims to understand the impact of the joint inversion in the presence of inconsistent discontinuities between the velocity model and the electrical model. From Fig. 5a1, due to the evanescent surface waves (longer period surface waves sample deeper structure with a much broader depth sensitivity kernel which results in a relatively poor depth resolution than shorter period), the inversion accuracy of the second layer is higher than that of the fourth one. In Fig. 5a2, a thick high conductivity layer emerges, which is similar to the real model. The discontinuities in velocity will not affect the inversion of the continuous low resistivity model by joint inversion. In the other situation when there exists two layers of low resistivity and a thick layer of low velocity, the cluster of the joint inversion results is concentrated near the real model (Fig. 5b1, b2). In Fig. 5b1, an obvious thick low velocity layer appears, indicating three layers of different resistivity. At the upper and lower coupling interfaces of the low velocity layer, two low resistivity layers appear in Fig. 5b2, which avoids the lack of accuracy in identifying two or more adjacent low resistivity layers by the MT method alone. Thus, we can conclude through the synthetic test that joint inversion can effectively retain the advantages of individual inversions when the discontinuities in

velocity and electrical models are inconsistent, while improving the inversion result by strengthening coupling during the process of joint inversion when the discontinuities of electrical conductivity and seismic velocity are consistent.

In the application of real data, four points on different blocks (eastern margin of the Tibetan Plateau, Sichuan Basin, middle and north segment of the fault) along the Longmenshan fault zone are tested to reveal the velocity and electrical models with the NSGA–SBX method. Point 1 (Fig. 9a) shows the eastern Tibetan Plateau with a high velocity and high resistivity layer in the shallow crust, two prominent mid-crustal low velocity layers and a high conductivity layer in the middle lower crust, which can be regarded as mechanical weakness. At point 2 (Fig. 9b), notably, a significant increase appears at  $\sim 8$  km in velocity and resistivity models, which probably indicates that the crustal channel flow terminates in the western margin. Point 3 (Fig. 9c) located on Sichuan Basin with much less deformation is characterized by low S-wave velocity and high conductivity in the shallow crust, with velocity increasing and conductivity decreasing with depth. This phenomenon is probably due to the thick sedimentary layers, since the Sichuan Basin is a part of the Yangtze craton which has been in a stable sedimentary environment. Point 4 located on the north segment of Longmenshan fault shows obviously different variations in velocity and electrical models (Fig. 9d). A high conductivity layer from  $\sim 8$  to  $\sim 20$  km is observed (Fig. 9d2), with velocity increasing with depth without any anomalies (Fig. 9d1). The cause of this high conductivity layer beneath point 4 might be the elevated fluid content of the fault zone. Compared with the previous studies with independent inversions, Li et al. (2009a, b)'s findings show two low velocity layers in the middle crust beneath the Tibetan Plateau and in the shallow crust beneath the Sichuan Basin. In MT analysis, Zhao et al. (2012) observed a high conductivity layer in the middle lower crust beneath the eastern Tibetan Plateau and a low resistivity layer near the surface in the Sichuan Basin. Peng et al. (2015) found a high conductivity layer in the shallow crust of the Sichuan Basin, whose conductivity decreases with depth, and a high conductivity layer in the middle lower crust

beneath the Songpan-Ganzi block. Our joint inversion results are consistent with these previous studies. However, because of the limitation of the independent method, the spatial distributions of the anomaly independently inverted from SWD and MT are not well consistent. Joint inversion can reconstruct the seismic velocity and electrical models at different depths towards converging inversion results. In the case of structurally similar velocity and electrical geological units, the resolution of velocity and electrical models can be improved when the models are met with the SWD and MT datasets at the same time. In Fig. 9b, c, the boundaries of the velocity models are almost in agreement with electrical models in point 2 and point 3. In other cases, from joint inversion results from point 1 and point 4, we find that the velocity model is inconsistent with resistivity due to the differences in sensitivity and resolution between independent SWD and MT methods. Joint inversion keeps the advantages of the individual methods when the discontinuities of the electrical and velocity models are inconsistent.

## 6. Conclusion

In this paper, we adopt an improved multi-objective genetic algorithm (NSGA–SBX) based on a global optimization approach to obtain results from joint inversion between surface wave dispersion curves and MT datasets. The integration of the different sources of information reduces the non-uniqueness of the solution and provides an improved seismic and electrical solution for complex geological conditions. Through comparison with the traditional genetic algorithm method, testing for the models with consistent and inconsistent boundaries, and applying the new inversion technique to the detection points around the Longmenshan fault zone, some main findings of this study can be summarized as follows:

1. Compared with the traditional binary encoding genetic process, the NSGA–SBX method yields better convergence results and avoids the lack of stability and precision caused by the selection of the discretization steps.

2. Joint inversion keeps the advantages of independent inversions when the discontinuities in velocity and electrical models are inconsistent, and can improve the inversion result with the NSGA-SBX method by strengthening structure coupling during the process of joint inversion when the discontinuities in electrical and velocity models are consistent.
3. In the application on the Longmenshan fault zone, we find that the Sichuan Basin demonstrates low S-wave velocity and high conductivity in the shallow crust, possibly due to thick sedimentary layers. The velocity increases and conductivity decreases with depth, which reflects the features of the stable Yangtze craton.
4. The eastern Tibetan Plateau demonstrates high velocity and high resistivity in the shallow crust, and two low velocity layers and a high conductivity layer in the middle-lower crust, probably indicating a mid-crustal channel flow. In addition, an extremely high resistivity layer beneath the middle segment (point 2) might be interpreted as the effects of southeast-directed crustal flow beneath eastern Tibet blocked by the rigid Sichuan Basin.
5. The velocity structure along the Longmenshan fault belt is consistent, while a high conductivity layer from  $\sim 8$  to  $\sim 20$  km is observed beneath the north segment, which might be caused by the elevated fluid content of the fault zone.

#### Acknowledgements

We would like to thank Dr. Li Hongyi for providing the group velocity dispersion data for this study. We also thank the editor and the anonymous reviewers whose comments and suggestions have contributed greatly to the improvement of the original manuscript. This study is supported by the National Science Foundation (NSF) of China (Grants 41704055).

#### REFERENCES

Arie, K., Adam, A., & Smythe, D. K. (1997). Combined seismic and magnetotelluric imaging of upper crystalline crust in the southern Bohemian massif. *First Break*, 15(8), 265–271.

- Cagniard, L. (1953). Basic theory of the magnetotelluric method of geophysical prospecting. *Geophysics*, 18(3), 605–635.
- Clark, M. K., & Royden, L. H. (2000). Topographic zone: Building the eastern margin of Tibet by lower crustal flow. *Geology*, 28, 703–706.
- Colombo, D., & Stefano, M. (2007). Geophysical modeling via simultaneous joint inversion of seismic, gravity, and electromagnetic data: Application to prestack depth imaging. *The Leading Edge*, 26(3), 326–331.
- Dobroka, M., Gyulai, A., Ormos, T., Csokas, J., & Dresen, L. (1991). Joint inversion of seismic and geoelectric data recorded in an underground coal mine. *Geophysical Prospecting*, 39(5), 643–665.
- Egbert, G. D., & Booker, J. R. (1992). Very long period magnetotellurics at Tucson observatory: Implication for mantle conductivity. *Journal of Geophysical Research*, 97(B11), 15113–15128.
- Gallardo, L. A., & Meju, M. A. (2003). Characterization of heterogeneous near-surface materials by joint 2-D inversion of dc resistivity and seismic data. *Geophysical Research Letters*, 30(13), 1658–1662.
- Gallardo, L. A., & Meju, M. A. (2004). Joint two-dimensional DC resistivity and seismic travel time inversion with cross-gradients constraints. *Journal of Geophysical Research*, 109(B3), 3311–3315.
- Kalyanmoy, D., & Agarwal, R. B. (1995). Simulated binary crossover for continuous search space. *Complex Systems*, 9, 115–148.
- Kalyanmoy, D., Pratap, A., Agarwal, S., & Meyarivan, T. (2002). A fast elitist multi-objective genetic algorithm: NSGA-II. *IEEE Transactions on Evolutionary Computation*, 6(2), 182–197.
- Knowles J, Corne D (1999) *The Pareto archived evolution strategy: A new baseline algorithm for multiobjective optimization*. In: Proceedings of the 1999 Congress on Evolutionary Computation. Piscataway, NJ: IEEE Press, pp. 98–105.
- Li, H. Y., Su, W., Wang, C. Y., & Huang, Z. X. (2009a). Ambient noise Rayleigh wave tomography in western Sichuan and eastern Tibet. *Earth and Planetary Science Letters*, 282, 201–211.
- Li, Y. H., Wu, Q. J., & Zhang, R. Q. (2009b). The lithospheric thinning of the North China Craton inferred from Rayleigh waves inversion. *Geophysical Journal International*, 177(3), 1334–1342.
- Liu, Q. Y., van der Hilst, R. D., Yao, H. J., Chen, J. H., Guo, B., et al. (2014). Eastward expansion of the Tibetan plateau by crustal flow and strain partitioning across faults. *Nature Geoscience*, 7(5), 361–365.
- Moorkamp, M., Jones, A., & Fishwick, S. (2011). Joint inversion of receiver functions, surface wave dispersion and magnetotelluric data. *Journal of Geophysical Research Solid Earth*, 115(B4), B04318.
- Nelson, K. D., Zhao, W., Brown, L. D., Kuo, J., et al. (1996). Partially molten middle crust beneath southern Tibet: Synthesis of project INDEPTH results. *Science*, 274, 1684–1688.
- Parker, R., & Booker, J. (1996). Optimal one-dimensional inversion and bounding of magnetotelluric apparent resistivity and phase measurements. *Physical Earth Planetary International*, 98, 269–282.
- Peng, M., Jiang, M., Tan, H. D., Li, Q. Q., Zhang, L. S., Xu, L. H., et al. (2015). Electrical structure of the crust beneath the central-northern segment of the LongMen Shan fault one and its geodynamic model. *Seismology and Geology*, 37(1), 162–175.

- Ritzwoller, M. H., & Levshin, A. L. (1998). Eurasian surface wave tomography: group velocities. *Journal of Geophysical Research*, *103*, 4839–4878.
- Roux, E., Moorkamp, M., & Jones, A. (2011). Joint inversion of long period magnetotelluric data and surface-wave dispersion curves for anisotropic structure: Application to data from Central Germany. *Geophysical Research Letters*, *38*(5), 05304–05309.
- Srinivas, N., & Deb, K. (2000). Multiobjective function optimization using nondominated sorting genetic algorithms. *Evolutionary Computation*, *2*(3), 221–248.
- Tikhonov, A. N. (1950). On the determination of electric characteristics of deep layers of the earth's crust. *Doklady Akademii Nauk*, *73*(2), 295–297.
- Wang, X. B., Zhu, Y. T., Zhao, X. K., et al. (2009). Deep conductivity characteristics of the Longmen Shan, Eastern Qinghai-Tibet Plateau. *Chinese Journal of Geophysics*, *52*(2), 564–571. (in Chinese).
- Wu, J. P., Huang, Y., Zhang, T. Z., Ming, Y. H., & Fang, L. H. (2009). After shock distribution of the Ms 8.0 Wenchuan earthquake and 3-D P wave velocity structure in and around source region. *Journal of Geophysics*, *52*(1), 102–111. (in Chinese).
- Wu, F. T., & Levshin, A. L. (1994). Surface wave group velocity tomography of East, Asia. *Physics of the Earth and Planetary*, *84*, 59–77.
- Zhao, G. Z., Unsworth, M. J., Zhan, Y., et al. (2012). Crustal structure and rheology of the Longmenshan and Wenchuan Mw 7.9 earthquake epicentral area from magnetotelluric data. *Geology*, *40*(12), 1139–1142.
- Zitzler, E. (1999). *Evolutionary algorithms for multiobjective optimization: Methods and applications*, Doctoral dissertation ETH 13398. Zurich: Swiss Federal Institute of Technology (ETH).

(Received July 18, 2017, revised April 5, 2018, accepted April 25, 2018, Published online May 4, 2018)